

Synthetic multi-dimensional Aharonov-Bohm cages in Fock state lattices

Jiajian Zhang,^{1,2,3,*} Wenhui Huang,^{1,2,3,*} Ji Chu,^{1,2,3} Jiawei Qiu,^{1,2,3} Xuandong Sun,^{1,2,3} Ziyu Tao,^{1,2,3} Jiawei Zhang,^{1,2,3} Libo Zhang,^{1,2,3} Yuxuan Zhou,^{1,2,3} Yuanzhen Chen,^{1,2,3,4} Yang Liu,^{1,2,3} Song Liu,^{1,2,3} Youpeng Zhong,^{1,2,3,†} Jian-Jian Miao,^{5,‡} Jingjing Niu,^{2,§} and Dapeng Yu^{1,2,3,4}

¹*Shenzhen Institute for Quantum Science and Engineering,
Southern University of Science and Technology, Shenzhen 518055, China*

²*International Quantum Academy, Shenzhen 518048, China*

³*Guangdong Provincial Key Laboratory of Quantum Science and Engineering,
Southern University of Science and Technology, Shenzhen 518055, China*

⁴*Department of Physics, Southern University of Science and Technology, Shenzhen 518055, China*

⁵*Department of Physics and HKU-UCAS Joint Institute for Theoretical and Computational Physics at Hong Kong,
The University of Hong Kong, Hong Kong, China*

Fock-state lattices (FSLs), composed of photon number states with infinite Hilbert space, have emerged as a promising platform for simulating high-dimensional physics due to their potential to extend into arbitrarily high dimensions. Here, we demonstrate the construction of multi-dimensional FSLs using superconducting quantum circuits. By controlling artificial gauge fields within their internal structures, we investigate flux-induced extreme localization dynamics, such as Aharonov-Bohm caging, extending from 2D to 3D. We also explore the coherent interference of quantum superposition states, achieving extreme localization within specific subspaces assisted by quantum entanglement. Our findings pave the way for manipulating the behavior of a broad class of quantum states in higher-dimensional systems.

By reinterpreting degrees of freedom in quantum systems as additional spatial dimensions, synthetic dimensions have emerged as a powerful tool for exploring high-dimensional physics [1–5], offering new insights and experimental possibilities beyond the constraints of traditional spatial dimensions [6–10]. A distinctive feature of synthetic dimensions is the ability to incorporate artificial gauge fields via site-dependent hopping [11–13], extending phenomena traditionally limited to charged particles, such as the Aharonov-Bohm (AB) effect [14–16], to neutral particles like photons [12, 17, 18]. This ability facilitates the exploration of quantum transport and localization dynamics under gauge fields within synthetic lattices. An intriguing phenomenon is AB caging, a flat-band localization effect [19–22] arising from the combined influence of local topology [23] and magnetic fields. Recent advancements in synthetic quantum systems have enabled the implementation of intricate lattice geometries [24, 25] and artificial gauge fields [26–31], making them ideal platforms for exploring AB caging in flat-band lattice. This phenomenon has been demonstrated in a variety of systems, including ion traps [32], photonic lattices [33–35], circuit quantum electrodynamics [36–38], topoelectrical circuits [39], ultracold atoms [40], and Rydberg lattices [37], etc.

Thus far, AB caging has been confined to two-dimensional (2D) systems, where wavefunctions are localized on finite subsets due to destructive interference, rather than exponential decay over the lattice sites. How-

ever, maintaining such extreme localization [41, 42] becomes increasingly difficult as the coordination increases in higher dimensions, where more pathways allow the wavefunction to spread. In a 3D lattice, for example, particles initially localized on a 2D plane can escape to perpendicular space through available pathways outside the plane. Achieving extreme localization, or AB caging, in higher-dimensional systems not only challenges the precision of quantum state manipulation but also offers a platform for controlling single-particle and multi-particle dynamics in arbitrary-dimensional spaces. Fock-state lattices (FSLs) [43–45], constructed from photon number states, offer a promising platform for simulating high-dimensional physics [46, 47]. One of their key advantages is the ability to accommodate both a minimal zero-photon state and an unrestricted size range, enabling the construction of high-dimensional lattice symmetries with flexible energy-level structures. Additionally, by synthesizing artificial gauge fields within FSLs, these systems provide a unique platform for investigating phenomena such as exotic topological phases with specific boundary conditions [48, 49], as well as extreme localization in high-dimensional spaces.

Superconducting quantum circuits [26, 50–56], comprising linear oscillators and non-linear Josephson junctions, provide a versatile platform for constructing synthetic FSLs and exploring high-dimensional quantum phenomena [46–48, 57]. In this work, we utilize superconducting qutrits to construct multi-dimensional synthetic FSLs, using 2D plaquettes as the building blocks. We demonstrate 2D AB caging on a single plaquette and extend this concept to 3D by incorporating two perpendicular rhombic plaquettes to form a 3D octahedral FSL. In this 3D system, localization arises from a distinct topological configuration formed by these two plaquettes with

* These authors contributed equally to this work.

† zhongyp@sustech.edu.cn

‡ mjphy@gmail.com

§ niujj@iqasz.cn

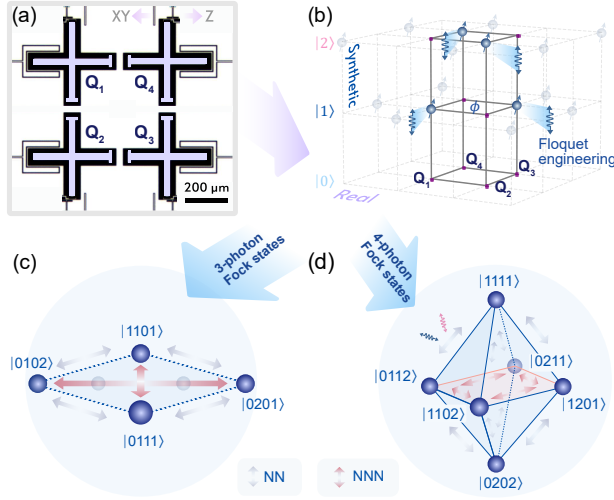


Fig. 1. Synthetic AB cage in multi-photon FSLs. (a) Photograph of the four-qutrit quantum processor. (b) Schematic of the experiment. The z -axis represents the eigenstates in synthetic space, with spin symbols marking the excited states in real space. The artificial gauge flux ϕ is synthesized via Floquet engineering of the qutrit frequencies. (c) Schematic of a 2D synthetic plaquette constructed with three-photon Fock states. (d) Schematic of a 3D synthetic octahedron constructed with four-photon Fock states. Blue arrows: NN coupling; red arrows: NNN coupling between qutrits.

both half a flux quantum embedded in 3D space. This extension is facilitated by the flexible energy-level configuration of qutrits, and we further show that the octahedral lattice can serve as a building block for constructing more complex FSLs involving additional qutrits. Given the challenges of directly simulating real 3D space, our demonstration of 3D AB caging within a synthetic FSL confirms the feasibility of simulating quantum physics in higher synthetic dimensions.

The synthetic AB cages are implemented on a device containing four superconducting qutrits Q_i ($i = 1 - 4$) of the transmon type [58], situated at corners of a plaquette and capacitively coupled to each other, as shown in Fig. 1(a). Extending the transmon Hilbert space to three levels allows us to engineer a broader range of synthetic lattice structures using fewer physical resources. Qudits offer even more theoretical advantages, but they pose more stringent requirements on microwave control and readout. The system's Hamiltonian is given by

$$\frac{H}{\hbar} = \sum_{i=1}^4 \left[\omega_i a_i^\dagger a_i + \frac{1}{2} U_i n_i (n_i - 1) \right] + \sum_{i < j} g_{ij} (a_i^\dagger a_j + a_j^\dagger a_i), \quad (1)$$

where a_i and $n_i = a_i^\dagger a_i$ denote the bosonic annihilation and particle number operators. We truncate each operator at two photons and obtain a four-qutrit system. For each qutrit Q_i , $\omega_i/2\pi$ is the resonant frequency between the lowest two eigenenergies, $U_i/2\pi \approx -216$ MHz represents the on-site attractive Hubbard interaction strength determined by the anharmonicity of the qutrit [59], and g_{ij} denotes the coupling strength between qutrits which

are directly coupled through their capacitor pads, resulting in nearest-neighbor (NN) coupling strengths $g_{12}/2\pi$, $g_{23}/2\pi$, $g_{34}/2\pi$, $g_{41}/2\pi \sim 14$ MHz, and next-nearest-neighbor (NNN) coupling strengths $g_{13}/2\pi$, $g_{24}/2\pi \sim 3.2$ MHz. The multiphoton FSLs formed by the eigenstates of the qutrits facilitate the construction of multi-dimensional geometric configurations with only a few physical components. An interior artificial gauge field is synthesized by Floquet engineering [60, 61], as illustrated in Fig. 1(b). This technique is implemented by applying periodic parametric driving to the qutrit on-site energy $\omega_i/2\pi$ through the Z control line. Under this driving, the system's physics is captured by the following effective Hamiltonian within the FSL:

$$H_{\text{eff}}/\hbar = \sum_{k < l} \left(J_{kl} e^{i\phi_{kl}} |\psi_k\rangle \langle \psi_l| + H.c. \right), \quad (2)$$

where J_{kl} denotes the effective hopping strength between states $|\psi_k\rangle$ and $|\psi_l\rangle$ at site k and l in synthetic space, tunable by the amplitude of the driving, and ϕ_{kl} is determined by the phase of the driving, see Ref. [62] for details. These phases from parametric driving yield synthetic magnetic flux invariant under gauge transformation $\Phi_C = \sum_C \phi_{kl}$ summed over the closed path of a Wilson loop C [63, 64].

We first illustrate the construction of a 2D plaquette using three-photon Fock states $|0111\rangle$, $|1101\rangle$, $|0102\rangle$, and $|0201\rangle$ as lattice sites $|\psi_k\rangle$ for $k = 1$ to 4, where Q_1 and Q_3 operate within the $\{|0\rangle, |1\rangle\}$ subspace, while Q_2 and Q_4 operate within the $\{|1\rangle, |2\rangle\}$ subspace, as illustrated in Fig. 1(c) (see details in Ref. [62]). Specifically, the qutrit frequencies $\omega_2/2\pi$ and $\omega_4/2\pi$, are quenched to approximately 4.91 GHz, while $\omega_1/2\pi$ and $\omega_3/2\pi$ are tuned to approximately 4.73 GHz, where the energy levels of $|11\rangle$ and $|02\rangle$ of each pair of NN qutrits are quenched to the vicinity of the operational frequencies [62], then the qutrit frequencies are modulated by parametric driving to establish the synthetic lattice. The nonlinearity U_i of our superconducting qutrits prevents state leakage outside this synthetic subspace. We can further extend this approach to explore higher-dimensional geometries, constructing a 3D lattice with four-photon Fock states: $|0202\rangle$, $|0112\rangle$, $|1201\rangle$, $|0211\rangle$, $|1102\rangle$, and $|1111\rangle$, forming an octahedral structure (Fig. 1(d)). Upon tuning the flux in the synthetic space via Floquet engineering, the states traversing different paths accumulate distinct phases, leading to constructive or destructive interference phenomena.

Now we present the experimental demonstration of AB caging in a 2D synthetic plaquette. The system is initialized in the three-photon Fock state $|\psi_1\rangle = |0201\rangle$ on a plaquette (Fig. 2(a)). The qutrits are then quenched to their operational frequencies to establish the synthetic space (Ref. [62] Sec. III). Subsequently, we apply parametric driving on all qutrits to form a dual-path interferometer. The NN hopping strengths ($J_{12}/2\pi$, $J_{23}/2\pi$, $J_{34}/2\pi$, $J_{41}/2\pi$) are tuned to ~ 18.4 MHz, and phase between lattice sites are adjusted by tuning the driving parameters

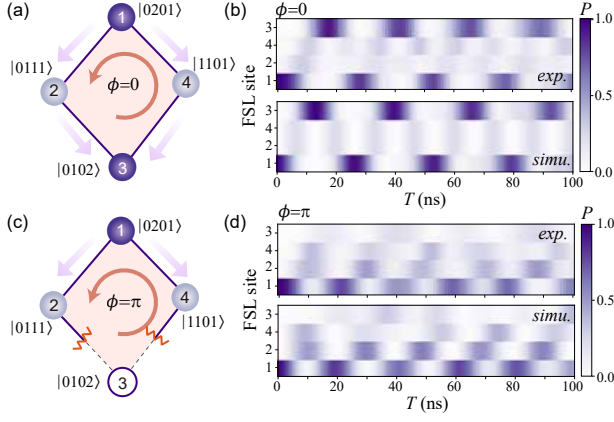


Fig. 2. (a) Diagram of a free quantum walk in a closed loop. (b) Constructive interference at $\phi = 0$, resulting in identical hopping rates through two paths. (c) Illustration of the AB cage phenomenon in a synthetic 2D plaquette. (d) Destructive interference at $\phi = \pi$, with hopping through both paths retained. The top and bottom panels in (b) and (d) display experimental data and numerical simulations, respectively.

on the two qutrits involved in the interaction between the $|11\rangle$ and $|02\rangle$ states (see details in Ref. [62]). When the synthetic flux $\phi = \phi_{12} + \phi_{23} + \phi_{34} + \phi_{41}$ is tuned to zero (Fig. 2(a)), i.e., by setting $\phi_{12} = \phi_{23} = \phi_{34} = \phi_{41} = 0$, and the transition strengths along the four paths are balanced, constructive interference results in a free quantum walk between the state $|0201\rangle$ at site 1 and state $|\psi_3\rangle = |0102\rangle$ at site 3, see the evolution of the site population P versus the evolution time T in Fig. 2(b). Conversely, when the synthetic flux is tuned to $\phi = \pi$ by adjusting $\phi_{12} = \phi_{23} = \pi/2$ and $\phi_{34} = \phi_{41} = 0$, destructive interference erases population at site 3 (see Figs. 2(c) and (d)). This extreme localization pattern confirms the establishment of an AB cage within 2D plaquette. The observed residual population at site 3 is attributed to experimental imperfections in the actual driving Hamiltonian (see Fig. 2(d) and Ref.[62], Sec. III.A.)

Next, we extend our synthetic framework beyond 2D. In real space, expanding the dynamics of AB cages typically requires increasing the number of atoms and altering their arrangement. However, in our synthetic FSL, this can be achieved by lifting the number of photons constituting the FSL. Specifically, we manipulate six Fock states of four-photon excitations in resonance: $|0202\rangle$, $|1201\rangle$, $|1102\rangle$, $|0211\rangle$, $|0112\rangle$, and $|1111\rangle$, sequentially labeled from synthetic sites 1 to 6, as depicted in Figs. 3(a) and (c). In this configuration, sites 1, 2, 3, and 6 form one plaquette, while sites 1, 4, 5, and 6 form another, encompassing both left-right and front-back paths. These two plaquettes share a common z -axis, resulting in a composite interference pattern that includes both the xz (blue) and yz (red) plaquettes. The synthetic flux exists in both plaquettes, jointly controlling the state transport behavior along the paths formed by the NN $|11\rangle - |02\rangle$ coupling. The fluxes are $\phi_{xz} = \phi_{12} + \phi_{26} + \phi_{63} + \phi_{31}$ and $\phi_{yz} = \phi_{14} + \phi_{46} + \phi_{65} + \phi_{51}$. The system is initial-

ized at site 1 ($|\psi_1\rangle = |0202\rangle$) with qutrits at idling frequencies. Frequency modulation, similar to the 2D AB cage experiment, establishes synthetic phases across the two plaquettes. When the flux within both plaquettes is set to zero, namely $\phi_{xz} = \phi_{yz} = 0$, and the hopping strengths along the four paths are balanced, we observe a free quantum walk between site 1 and site 6 ($|1111\rangle$), as demonstrated in Fig. 3(b). Conversely, setting $\phi_{xz} = \phi_{yz} = \pi$, by tuning $\phi_{12} = \phi_{63} = \phi_{46} = \phi_{51} = \pi/2$, and $\phi_{26} = \phi_{31} = \phi_{14} = \phi_{65} = 0$, induces destructive interference across all four paths, leading to localization on site 1 (Fig. 3(d)). Experimental results align well with numerical simulations, the slight distortions appear at sites 2, 3, 4, and 5 could be caused by imbalanced hopping strengths across all four paths during parametric modulation. The desynchronization of probability distribution along different paths and slight delocalization on site 6 are likely caused by both the disorder in hopping strength and phase mismatch due to shifts in energy levels when modulating the phase of parametric driving pulses (see [62] Fig.S10 for numerical simulation analysis). To mitigate these effects, we have slightly decreased the parametric drive amplitude in this scenario.

The extension towards pseudo-3D demonstrates that synthetic magnetic fields can still be simultaneously controlled within an expanded synthetic space. However, this verification is limited to the combined effects of interference paths, similar to the 2D scenario. Our next step will utilize quantum coherence and superposition to explore the richer dynamics within a genuine 3D cage. By activating NNN coupling, we extend the dual-plaquette structure into a complete 3D octahedral configuration, as illustrated in Fig. 3(e). Careful tuning of the resonance positions of synthetic sites 2, 3, 4, and 5 establishes NNN hopping among these sites, forming a plaquette perpendicular to the z -axis, termed the xy plaquette. This equatorial plaquette comprises sites 2, 3, 4, and 5 (left in Fig. 3(e)), with NNN hopping strengths satisfying $J_{24} = J_{35} = J_{25}/2 = J_{34}/2$, where $J_{34}/2\pi \sim 5.7$ MHz, making this octahedron “skewed”, see [62] for details. Previously, we have discussed the dynamics in 2D plaquettes with the system initialized at a single site, showing the features of a multi-path interferometer but only resulting in dynamics and localization at a single site. A full exhibition of 3D AB caging requires the capability of localization on a plane. To manifest this feature, we initialize the system in a quantum entangled state within the synthetic 3D FSL to directly control the superposition state interference and explore caging dynamics distinguished from the 2D cases.

To experimentally realize this, we initialize the system in the superposition state at sites 2 and 3: $|\psi_0\rangle = \frac{1}{\sqrt{2}}(|0112\rangle + |1201\rangle)$, as shown in Fig. 3(e). Subsequently, we apply parametric driving to the qutrits similar to the previous experiments. We first focus on the xz plane (comprising sites 1, 2, 3, and 6). By setting $\phi_{12} = \phi_{63} = \pi$ and $\phi_{26} = \phi_{31} = 0$, the plaquette is divided into two triangular regions, each containing a π synthetic flux (middle

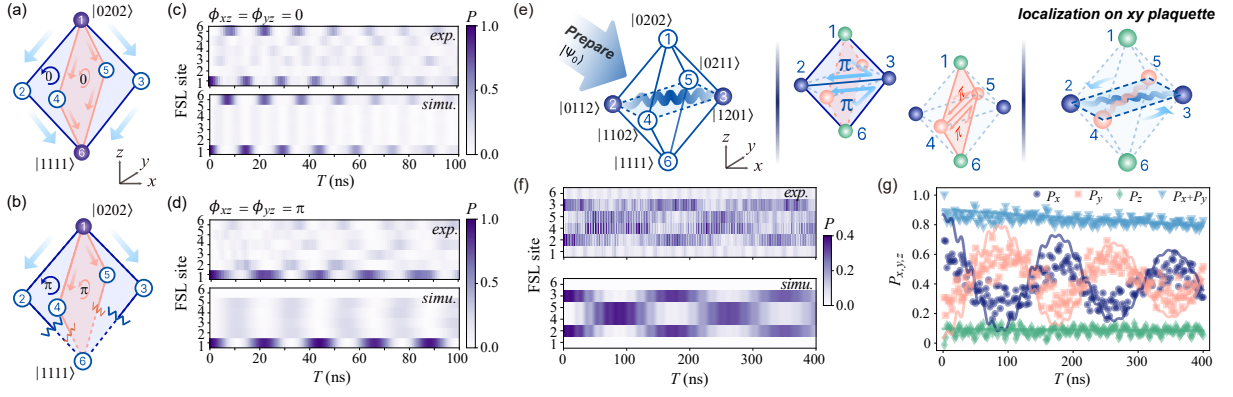


Fig. 3. (a) Schematic of two plaquettes with a common z -axis, the sites 1 – 6 represent the states $|0202\rangle$, $|0112\rangle$, $|1201\rangle$, $|0211\rangle$, and $|1111\rangle$, respectively. (b) Pseudo-3D AB cage with flux in both plaquettes set to π . (c) Evolution dynamics among the six sites, akin to the 2D plaquette. With flux in both plaquettes set to zero, a free quantum walk through four paths occurs, resulting in state transfer between $|0202\rangle$ and $|1111\rangle$. (d) Destructive interference along the z -axis, leading to population cancellation at $|1111\rangle$. (e) Schematic of 3D AB cage dynamics on a skewed octahedral FSL. Left: Initialization to a two-site superposition state, $|\Psi_4\rangle = \frac{1}{\sqrt{2}}(|0112\rangle + |1201\rangle)$. Middle: Two vertical plaquettes each trapping a π flux within two triangular regions, resulting in destructive interference for both plaquettes. Right: Photon evolution is confined to the equatorial section of the 3D AB cage. (f) Evolution dynamics among the six sites in the 3D AB cage. The top and bottom panels in (c), (d), and (f) show experimental data and numerical simulations, respectively. (g) Evolution of probabilities $P_{x,y,z}$, illustrating the localization pattern. Dots: experimental results; solid curves: numerical simulations.

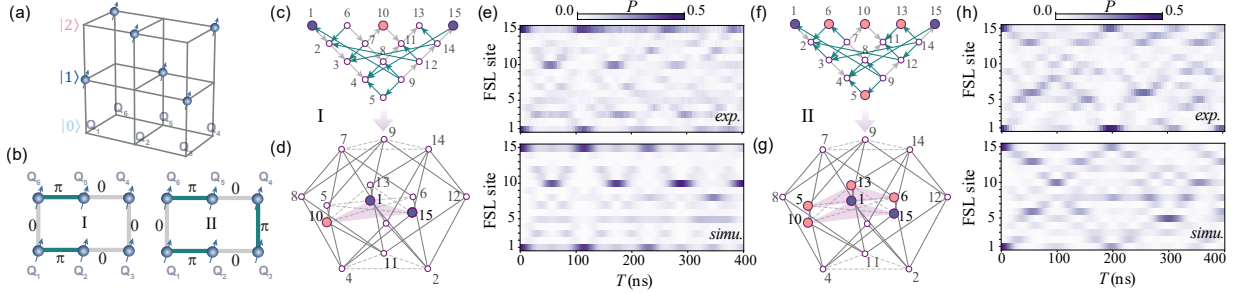


Fig. 4. (a) Energy level configuration of the 6-qutrit loop. (b) Flux modulation configurations (I and II) on the loop edges. (c-d) Synthetic FSL formed in the two-excitation subspace with flux configuration I. Solid lines: NN coupling; dashed lines: NNN coupling. Blue circles: initial sites; pink circles: sites with positive superposition in different interference paths. (c) synthetic sites and NN coupling, (d) effective FSL folded by the actual coupling strengths. (e) Dynamics of superposition state $|\Psi_6\rangle = (|120101\rangle + |010112\rangle)/\sqrt{2}$ in the FSL from (c). (f-g) Synthetic FSL with flux configuration II. (h) Dynamics of $|\Psi_6\rangle$ in FSL from (f). Upper and lower panels in (e) and (h) show experimental data and numerical simulations, respectively.

in Fig. 3(e)). As a consequence, the superposition state becomes confined at sites 2 and 3. Applying the same phase modulation process to the yz plaquette confines the system to the superposition state at sites 4 and 5, and the combined modulations on xz and yz plaquettes freeze the dynamical evolution along the z axis. Within these operations, we adjust the operational frequencies of four qutrits to keep sites 1–6 in resonance, therefore no extra flux is trapped inside the xy plaquette. The NNN coupling induces constructive interference at sites 2, 3, 4, and 5, as shown in the lower panel of Fig. 3(f), the synchronized dynamics between sites 2, 3 and sites 4, 5 with evolution time T , indicates that quantum superposition is coherently maintained in this 3D AB cage. This coherent localization behavior can also be understood by the FSL site population projected on three directions,

where the x -component, $P_x = P_2 + P_3$, and y -component, $P_y = P_4 + P_5$, undergo typical vacuum Rabi oscillations, here P_k means the population of state $|\psi_k\rangle$ at site k . The combined quantity $P_x + P_y$ characterizes the distribution of localized states in the xy plaquette (right in Fig. 3(g)), while the z -component ($P_z = P_1 + P_6$) remains low occupation, indicating that the residual distribution outside the xy plaquette is extremely caged. These experimental results demonstrate the successful synthesis of magnetic flux across two longitudinal sections (xz and yz plaquettes) within a 3D AB cage, which effectively localizes a quantum superposition state within the xy plaquette. This effect provides evidence for the realization of a genuine 3D AB cage with the assistance of NNN coupling.

Our method demonstrates a promising feature that more complex FSLs can be synthesized with only a few

physical resources. As an example, we extend our investigation to six qutrits on another quantum processor (see Ref. [62] Fig.S14). The operational frequencies of the NN qutrits are staggered (see Fig. 4(a)), in the same approach as the previous experiment, facilitating the formation of hopping terms through 11 – 02 coupling. The phase of each coupling between two qutrits is independently tunable. The system’s ground state is $|010101\rangle$, with higher-frequency qutrits initialized to $|1\rangle$. Based on this ground state, the FSL consists of 15 two-excitation Fock states, labeled as sites 1 to 15: $|120101\rangle$, $|111101\rangle$, $|110201\rangle$, $|110111\rangle$, $|110102\rangle$, $|021101\rangle$, $|020201\rangle$, $|020111\rangle$, $|020102\rangle$, $|011201\rangle$, $|011111\rangle$, $|011102\rangle$, $|010211\rangle$, $|010202\rangle$, and $|010112\rangle$ (see Ref. [62] Section IV.A). The dynamics of these states are governed by coherent interference modulated by the applied flux configurations. We illustrate two specific flux configurations, I and II, in Fig. 4(b), with corresponding state distributions in Fig. 4(c) and (f). The system begins in a superposition of sites 1 and 15, marked by solid blue circles. Arrows in Fig. 4(c) and (f) indicate the phase direction of multi-path interference (see Ref. [62] Fig. S15). The Figs. 4(d) and (g) show 3D projections of the FSL, where edge lengths correspond to the actual coupling strengths. In flux configuration I, multi-path interference leads to a periodic positive superposition at site 10 (Fig. 4(e)), while populations at most other sites are canceled by destructive interference. The dynamics are thus localized in a “plane” formed by sites 1, 10 and 15 (marked in pink in Fig. 4(d)). In flux configuration II, periodic superpositions occur at sites 5, 6, 10, and 13 (Fig. 4(h)), forming a localized subspace consisting of two “planes” (marked in pink in Fig. 4(g)). These patterns can be understood as arising from multiple paths connecting the entangled states at sites 1 and 15, resulting in localization within subspaces of FSL sites with NN couplings (see Ref. [62], Section IV.B). Additionally, we examine the evolution and interference when the system is initialized at single FSL sites, 1 or 15 (see

Section IV.C of Ref. [62]). These results further demonstrate the ability of our approach to construct subspaces of compact localized states in more complex FSLs.

In conclusion, our work demonstrates the construction of multi-dimensional FSLs using superconducting qutrits. Utilizing Floquet engineering and tunable coupler, we effectively manipulate coupling strengths and create synthetic gauge fields in multi-photon FSLs, allowing us to explore gauge field-induced extreme localization dynamics such as AB caging from 2D to 3D. We also investigate the coherent interference of quantum superposition states, achieving extreme localization within specific subspaces of multi-dimensional AB cages, facilitated by quantum entanglement. Our work opens a pathway to localize a large family of states on FSLs under gauge fields in higher-dimensional systems, leveraging the internal degrees of freedom inherent in quantum platforms. This approach could be useful for studying quantum many-body systems, such as perovskite materials with high-temperature superconductivity [65, 66] and giant magnetoresistance [67], topological edge states [68, 69], and quantum chaos [70].

ACKNOWLEDGMENTS

This work was supported by the National Natural Science Foundation of China (12174178, 12204228, 12374474), the Guangdong Provincial Key Laboratory (2019B121203002), the Science, Technology and Innovation Commission of Shenzhen Municipality (KQTD20210811090049034, K21547502), the Shenzhen-Hong Kong Cooperation Zone for Technology and Innovation (HZQB-KCZYB-2020050), and the Guangdong Basic and Applied Basic Research Foundation (2022A1515110615, 2024A1515011714). J. J. Miao was supported by General Research Fund Grant No. 14302021 from Research Grants Council of Hong Kong.

-
- [1] O. Boada, A. Celi, J. I. Latorre, and M. Lewenstein, *Phys. Rev. Lett.* **108**, 133001 (2012).
 - [2] M. Lohse, C. Schweizer, H. M. Price, O. Zilberberg, and I. Bloch, *Nature* **553**, 55 (2018).
 - [3] O. Zilberberg, S. Huang, J. Guglielmon, M. Wang, K. P. Chen, Y. E. Kraus, and M. C. Rechtsman, *Nature* **553**, 59 (2018).
 - [4] J.-B. Bouhiron, A. Fabre, Q. Liu, Q. Redon, N. Mittal, T. Sator, R. Lopes, and S. Nascimbene, *Science* **384**, 223 (2024).
 - [5] Q. Lin, X.-Q. Sun, M. Xiao, S.-C. Zhang, and S. Fan, *Sci. Adv.* **4** (2018).
 - [6] E. Lustig, S. Weimann, Y. Plotnik, Y. Lumer, M. A. Bandres, A. Szameit, and M. Segev, *Nature* **567**, 356 (2019).
 - [7] T. Ozawa and H. M. Price, *Nat. Rev. Phys.* **1**, 349 (2019).
 - [8] A. Dutt, Q. Lin, L. Yuan, M. Minkov, M. Xiao, and S. Fan, *Science* **367**, 59 (2020).
 - [9] Z.-C. Xiang, K. Huang, Y.-R. Zhang, T. Liu, Y.-H. Shi, C.-L. Deng, T. Liu, H. Li, G.-H. Liang, Z.-Y. Mei, *et al.*, *Nat. Commun.* **14** (2023).
 - [10] J. Argüello-Luengo, U. Bhattacharya, A. Celi, R. W. Chhajlany, T. Grass, M. Płodzień, D. Rakshit, T. Salamon, P. Stornati, L. Tarruell, and M. Lewenstein, *Commun. Phys.* **7** (2024).
 - [11] A. Celi, P. Massignan, J. Ruseckas, N. Goldman, I. B. Spielman, G. Juzeliūnas, and M. Lewenstein, *Phys. Rev. Lett.* **112**, 043001 (2014).
 - [12] L. D. Tzuang, K. Fang, P. Nussenzveig, S. Fan, and M. Lipson, *Nat. Photon.* **8**, 701 (2014).
 - [13] K. Fang, Z. Yu, and S. Fan, *Nat. Photon.* **6**, 782 (2012).
 - [14] Y. Aharonov and D. Bohm, *Phys. Rev.* **115**, 485 (1959).
 - [15] D. Jaksch and P. Zoller, *New J. Phys.* **5**, 56 (2003).
 - [16] J. Dalibard, F. Gerbier, G. Juzeliūnas, and P. Öhberg, *Rev. Mod. Phys.* **83**, 1523 (2011).
 - [17] L. Lu, J. D. Joannopoulos, and M. Soljačić, *Nat. Photon.*

- 8, 821 (2014).
- [18] T. Ozawa, H. M. Price, A. Amo, N. Goldman, M. Hafezi, L. Lu, M. C. Rechtsman, D. Schuster, J. Simon, O. Zeitler, and I. Carusotto, *Rev. Mod. Phys.* **91**, 015006 (2019).
 - [19] J. Vidal, R. Mosseri, and B. Douçot, *Phys. Rev. Lett.* **81**, 5888 (1998).
 - [20] J. Vidal, B. Douçot, R. Mosseri, and P. Butaud, *Phys. Rev. Lett.* **85**, 3906 (2000).
 - [21] J. Vidal, P. Butaud, B. Douçot, and R. Mosseri, *Phys. Rev. B* **64**, 155306 (2001).
 - [22] R. Mosseri, R. Vogeler, and J. Vidal, *Phys. Rev. B* **106**, 155120 (2022).
 - [23] B. Sutherland, *Phys. Rev. B* **34**, 5208 (1986).
 - [24] J. M. Koh, T. Tai, and C. H. Lee, *Nat. Commun.* **15** (2024).
 - [25] L. Yuan, Q. Lin, M. Xiao, and S. Fan, *Optica* **5**, 1396 (2018).
 - [26] P. Roushan, C. Neill, A. Megrant, Y. Chen, R. Babbush, R. Barends, B. Campbell, Z. Chen, B. Chiaro, A. Dunsworth, *et al.*, *Nat. Phys.* **13**, 146 (2017).
 - [27] Y. Li, H. Du, Y. Wang, J. Liang, L. Xiao, W. Yi, J. Ma, and S. Jia, *Nat. Commun.* **14** (2023).
 - [28] Y. Wang, Y.-K. Wu, Y. Jiang, M.-L. Cai, B.-W. Li, Q.-X. Mei, B.-X. Qi, Z.-C. Zhou, and L.-M. Duan, *Phys. Rev. Lett.* **132**, 130601 (2024).
 - [29] J. S. C. Hung, J. H. Busnaina, C. W. S. Chang, A. M. Vadiraj, I. Nsanzineza, E. Solano, H. Alaeian, E. Rico, and C. M. Wilson, *Phys. Rev. Lett.* **127**, 100503 (2021).
 - [30] S. K. Kanungo, J. D. Whalen, Y. Lu, M. Yuan, S. Dasgupta, F. B. Dunning, K. R. A. Hazzard, and T. C. Killian, *Nat. Commun.* **13** (2022).
 - [31] T. Chen, C. Huang, I. Velkovsky, K. R. A. Hazzard, J. P. Covey, and B. Gadway, *Nat. Commun.* **15** (2024).
 - [32] A. Bermudez, T. Schaetz, and D. Porras, *Phys. Rev. Lett.* **107**, 150501 (2011).
 - [33] S. Longhi, *Opt. Lett.* **39**, 5892 (2014).
 - [34] S. Mukherjee, M. Di Liberto, P. Öhberg, R. R. Thomson, and N. Goldman, *Phys. Rev. Lett.* **121**, 075502 (2018).
 - [35] M. Kremer, I. Petrides, E. Meyer, M. Heinrich, O. Zeitler, and A. Szameit, *Nat. Commun.* **11**, 907 (2020).
 - [36] J. G. Martinez, C. S. Chiu, B. M. Smitham, and A. A. Houck, *Sci. Adv.* **9** (2023).
 - [37] T. Chen, C. Huang, I. Velkovsky, T. Ozawa, H. Price, J. P. Covey, and B. Gadway, [arXiv:2404.00737](https://arxiv.org/abs/2404.00737).
 - [38] I. T. Rosen, S. Muschinske, C. N. Barrett, A. Chatterjee, M. Hays, M. A. DeMarco, A. H. Karamlou, D. A. Rower, R. Das, D. K. Kim, *et al.*, *Nat. Phys.* (2024).
 - [39] W. Zhang, H. Wang, H. Sun, and X. Zhang, *Phys. Rev. Lett.* **130**, 206401 (2023).
 - [40] H. Li, Z. Dong, S. Longhi, Q. Liang, D. Xie, and B. Yan, *Phys. Rev. Lett.* **129**, 220403 (2022).
 - [41] M. Cherdantsev, K. Cherednichenko, and S. Cooper, *SIAM J. Math. Anal.* **50**, 5825 (2018).
 - [42] M. Röntgen, C. V. Morfonios, and P. Schmelcher, *Phys. Rev. B* **97**, 035161 (2018).
 - [43] J. Deng, H. Dong, C. Zhang, Y. Wu, J. Yuan, X. Zhu, F. Jin, H. Li, Z. Wang, H. Cai, *et al.*, *Science* **378**, 966 (2022).
 - [44] P. Saugmann and J. Larson, *Phys. Rev. A* **108**, 033721 (2023).
 - [45] J. Yuan, H. Cai, and D.-W. Wang, *Adv. Phys. X* **9** (2024).
 - [46] D.-W. Wang, H. Cai, R.-B. Liu, and M. O. Scully, *Phys. Rev. Lett.* **116**, 220502 (2016).
 - [47] Y. Yao, L. Xiang, Z. Guo, Z. Bao, Y.-F. Yang, Z. Song, H. Shi, X. Zhu, F. Jin, J. Chen, *et al.*, *Nat. Phys.* **19**, 1459 (2023).
 - [48] H. Cai and D.-W. Wang, *Natl. Sci. Rev.* **8** (2020).
 - [49] N. Mohanta, R. Soni, S. Okamoto, and E. Dagotto, *Commun. Phys.* **6** (2023).
 - [50] R. Ma, B. Saxberg, C. Owens, N. Leung, Y. Lu, J. Simon, and D. I. Schuster, *Nature* **566**, 51 (2019).
 - [51] D.-W. Wang, C. Song, W. Feng, H. Cai, D. Xu, H. Deng, H. Li, D. Zheng, X. Zhu, H. Wang, *et al.*, *Nat. Phys.* **15**, 382 (2019).
 - [52] Z. Yan, Y.-R. Zhang, M. Gong, Y. Wu, Y. Zheng, S. Li, C. Wang, F. Liang, J. Lin, Y. Xu, *et al.*, *Science* **364**, 753 (2019).
 - [53] M. Gong, S. Wang, C. Zha, M.-C. Chen, H.-L. Huang, Y. Wu, Q. Zhu, Y. Zhao, S. Li, S. Guo, *et al.*, *Science* **372**, 948 (2021).
 - [54] B. Saxberg, A. Vrajitoarea, G. Roberts, M. G. Panetta, J. Simon, and D. I. Schuster, *Nature* **612**, 435 (2022).
 - [55] A. Morvan, T. Andersen, X. Mi, C. Neill, A. Petukhov, K. Kechedzhi, D. Abanin, A. Michailidis, *et al.*, *Nature* **612**, 240 (2022).
 - [56] Z. Tao, W. Huang, J. Niu, L. Zhang, Y. Ke, X. Gu, L. Lin, J. Qiu, X. Sun, X. Yang, *et al.*, [arXiv:2303.04582](https://arxiv.org/abs/2303.04582).
 - [57] K. Zhang, H. Li, P. Zhang, J. Yuan, J. Chen, W. Ren, Z. Wang, C. Song, D.-W. Wang, H. Wang, *et al.*, *Phys. Rev. Lett.* **128**, 190502 (2022).
 - [58] J. Niu, L. Zhang, Y. Liu, J. Qiu, W. Huang, J. Huang, H. Jia, J. Liu, Z. Tao, W. Wei, *et al.*, *Nat. Electron.* **6**, 235 (2023).
 - [59] J. Koch, T. M. Yu, J. Gambetta, A. A. Houck, D. I. Schuster, J. Majer, A. Blais, M. H. Devoret, S. M. Girvin, and R. J. Schoelkopf, *Phys. Rev. A* **76**, 042319 (2007).
 - [60] J. H. Shirley, *Phys. Rev.* **138**, B979 (1965).
 - [61] T. Oka and S. Kitamura, *Annu. Rev. Condens. Ma. P.* **10**, 387 (2019).
 - [62] See Supplemental Material at [url] for the system parameters and experimental details.
 - [63] K. G. Wilson, *Phys. Rev. D* **10**, 2445 (1974).
 - [64] X. Wang, H.-R. Li, and F.-L. Li, *New J. Phys.* **22**, 033037 (2020).
 - [65] J. G. Bednorz and K. A. Müller, *Rev. Mod. Phys.* **60**, 585 (1988).
 - [66] Y. Maeno, H. Hashimoto, K. Yoshida, S. Nishizaki, T. Fujita, J. G. Bednorz, and F. Lichtenberg, *Nature* **372**, 532 (1994).
 - [67] Y. Moritomo, A. Asamitsu, H. Kuwahara, and Y. Tokura, *Nature* **380**, 141 (1996).
 - [68] F. Schindler, A. M. Cook, M. G. Vergniory, Z. Wang, S. S. P. Parkin, B. A. Bernevig, and T. Neupert, *Sci. Adv.* **4** (2018).
 - [69] B. Xie, H.-X. Wang, X. Zhang, P. Zhan, J.-H. Jiang, M. Lu, and Y. Chen, *Nat. Rev. Phys.* **3**, 520 (2021).
 - [70] J. Šuntajs, J. Bonča, T. Prosen, and L. Vidmar, *Phys. Rev. E* **102**, 062144 (2020).